Radiation energetics of inertial confinement fusion relevant wire-array z pinches

D.B. Sinars,[1] R.W. Lemke,[1] M.E. Cuneo,[1] S.V. Lebedev,[2] E.M. Waisman,[1] W.A. Stygar,[1] B. Jones,[1] M.C. Jones,[1] E.P. Yu,[1] J.L. Porter,[1] and D.F. Wenger[1]

[1]*Sandia National Laboratories, P.O. Box 5800, Albuquerque, NM 87185*
[2]*Blackett Laboratory, Imperial College, London SW7 2BW, United Kingdom*

(Dated: September 21, 2007)

Short implosion-time 20-mm diameter, 300-wire tungsten arrays maintain high peak x-ray powers despite a reduction in peak current from 19 to 13 MA. The main radiation pulse on tests with a 1-mm on-axis rod may be explained by the observable $\vec{j} \times \vec{B}$ work done during the implosion, but bare-axis tests require sub-mm convergence of the magnetic field not seen except perhaps in > 1 keV emission. The data includes the first measurement of the imploding mass density profile of a wire-array z-pinch and strongly constrains simulation models.

PACS numbers: 52.59.Qy,52.58.Lq,52.70.La,52.80.Qj

The idea of using cylindrical liner implosions driven by electromagnetic forces to produce high-intensity radiation sources has been around for decades [1]. Significant progress in this area in recent years has been made using $\sim$0.1 μs generators to create "fast" z-pinch implosions with cylindrical wire arrays [2]. The largest fast z-pinch facility today is the Sandia Z-machine [3], a 20-MA, 100-ns, 11 MJ pulsed power facility that has been used to produce >200 TW and 1-2 MJ of soft x rays (0.1-10 keV range) [3–6]. One application of these sources being evaluated is inertial confinement fusion (ICF) [7].

The premise behind z-pinch plasma radiation sources is that the radiation energy is produced by the cylindrical implosion and compression of the mass by the Lorentz $\vec{j} \times \vec{B}$ force [1]. However, the total energy radiated by Al z-pinch plasmas on 7 MA facilities was in excess of the estimated kinetic energy of the implosion by factors of 2-4 in some cases (see Ref. 8 and references therein). Early two-dimensional simulations of 40-mm diameter tungsten array experiments [9] explained the total radiation pulse as a combination of the implosion kinetic energy and subsequent additional plasma compression applied by the $\vec{j} \times \vec{B}$ force during stagnation. Even there, however, very large convergence ratios for the magnetic field (>20) were required in many cases to obtain a match with experimental radiation powers with no systematic experimental data to support or contradict such claims.

In this Letter we estimate the $\vec{j} \times \vec{B}$ work done and plasma convergence using multiple diagnostics that include the first direct measurement of the imploding mass density profile of a wire-array z-pinch. In tests with a 1-mm on-axis rod we find that the radiation can be readily explained by the observable $\vec{j} \times \vec{B}$ work, but bare-axis tests require the equivalent of sub-mm convergence of the magnetic field. Sub-mm convergence of the magnetic field is inconsistent with the plasma size seen in soft x-ray diagnostics except at >1 keV energies. The systematic data presented here provides a strong constraint on simulations beyond simply matching the radiation power, as illustrated by an example simulation of an array-on-rod experiment.

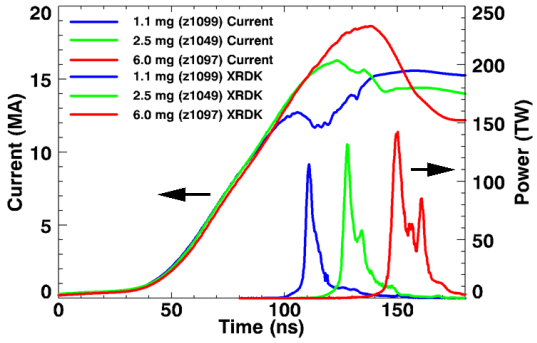

FIG. 1: Example load current and radiation power traces from the three different wire array masses studied here.

In this work we studied 20-mm diameter, 300-wire tungsten arrays on the Z-machine. By varying the initial wire diameter from 5.0 to 11.5 μm we changed the array mass from 1.1 to 6.0 mg and consequently changed the implosion time and the peak current as shown in Fig. 1. The arrays were placed in 30-mm diameter return-current canisters as described in Ref. 10. Previous related work studied 20-mm diameter, 300-wire tungsten arrays at 13 and 19 MA at a fixed 95 ns implosion time [11, 12].

The origin of the the main x-ray pulse is of interest for ICF applications. X rays emitted after the main radiation burst (here $\sim$50% total energy) are not useful for ICF. We define the main radiation pulse as all radiation inside and prior to the full-width at half-maximum (FWHM) of the main radiation burst. The FWHMs decrease with decreasing mass and are 4.5, 4.6, and 6.2 ns for the pulses shown in Fig. 2. The average energy in the main x-ray pulse, summarized in Table I, increases with increasing mass, as does the total energy radiated. One additional shot was done at each mass, in which a 1-mm diameter Al 5056 rod (21 mg) was inserted on the array axis. The radiation powers from these tests had comparable FWHMs to the bare-axis pinches but the peak

TABLE I: Summary of radiated energy and other parameters for the data in Fig. 2.

Array Mass	E_{main} (kJ)	E_{total} (kJ)	E^{rod}_{main} (kJ)	E^{rod}_{total} (kJ)	τ_{imp} (ns)	τ_{rise} (ns)	E_m/I^2_{max} (kJ/MA^2)	P_m/I^2_{max} (TW/MA^2)
1.1 mg	440±28	832±21	240	488	66.6±1.2	3.1±0.2	2.50±0.16	0.62±0.13
2.5 mg	532±46	1106±106	306	667	80.8±1.3	3.6±0.4	2.08±0.25	0.47±0.06
6.0 mg	692±66	1278±239	428	804	100.6±1.8	4.2±0.3	1.85±0.27	0.31±0.07

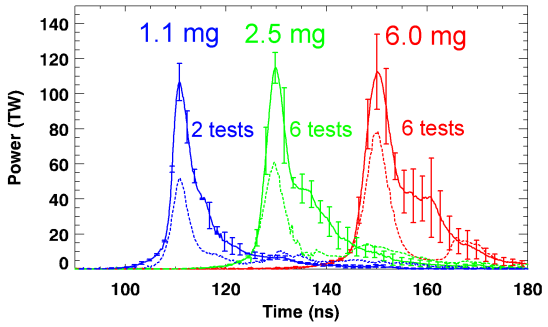

FIG. 2: Average of the Kimfol-filtered x-ray diode radiation powers for all shots with each mass plotted with standard deviations (solid). Also plotted are the powers from tests with a 1-mm diameter Al rod on the axis (dashed). (1.1 mg array-on-rod data is V-filtered due to loss of Kimfol data.)

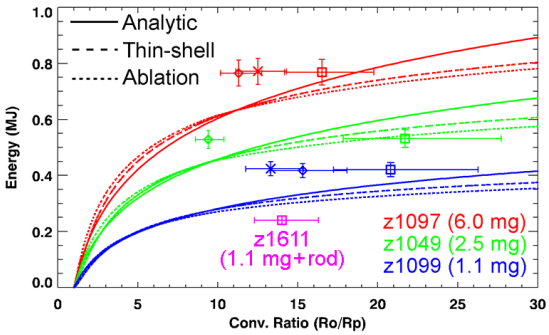

FIG. 3: Calculated $\vec{j} \times \vec{B}$ work vs. axially-averaged convergence ratio (CR) for example shots at each mass using three different models. For each shot the plasma CR inferred from pinhole camera (□), TGS (◇), and GIK (x) data is shown.

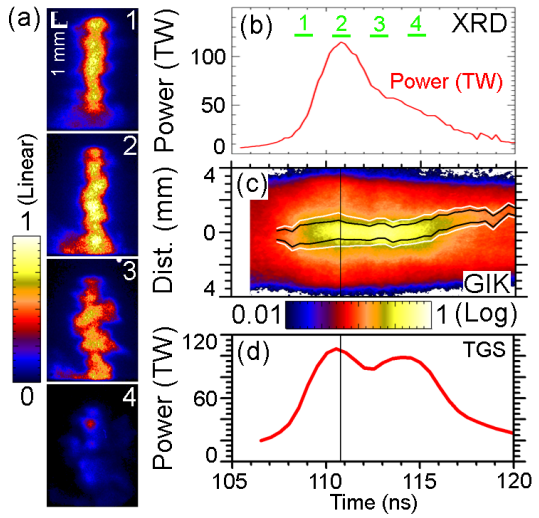

FIG. 4: Data from a 1.1 mg array implosion (z1099). (a) Gated pinhole camera data (12.7 μm Be filter, 200 μm pinhole, ~400 μm resolution). (b) Pinhole image timing relative to x-ray diode signal. (c) Streaked grazing-incidence mirror camera data showing axially-averaged, radially-resolved emission in 375-450 eV range. (d) Time-resolved power inferred from a transmission-grating spectrometer.

powers were about 1.75 times lower, with a larger reduction immediately following the main pulse.

Ref. 2 states that implosions should occur in a self-similar fashion if the parameter $\Pi = \mu I^2_{max} \tau^2/(4\pi m R_0^2)$ is the same, where I_{max} is the peak current, τ is the array implosion time, m is the array mass/length, and R_0 is the array radius. For the array masses in our study, $\langle \Pi_6 \rangle$=6.47, $\langle \Pi_{2.5} \rangle$=6.85, $\langle \Pi_{1.1} \rangle$=6.84. Our time- and amplitude-normalized current pulses are self-similar because of the linear rate of rise of the current, and the 10-90% rise time in of the radiation (Table I) scales linearly with τ for these arrays. Ref. 2 derives a convenient approximation for the $\vec{j} \times \vec{B}$ work done in J/m to a thin shell containing the total array mass,

$$W_{kin} = \frac{f\mu_0}{4\pi} I^2_{max} \ln\left(\frac{R_0}{R_p}\right), \quad (1)$$

where R_p is the final radius of the pinch and f is a current shape form factor. As shown in Fig. 3, the value f=0.76 gives the most similar results over the range of interest to 1-D thin-shell and ablation model calculations [10, 13, 14] incorporating a circuit model. The circuit-model calculations are more accurate in that they self-consistently limit the current as the z-pinch inductance increases.

An important feature of Eq. 1 is that the $\vec{j} \times \vec{B}$ work, and thus the expected radiation yield, depends only on I^2_{max} and the magnetic field convergence ratio (R_0/R_p). The similarity of the Π values nominally suggest similar normalized dynamics and convergence ratios, so that it might be expected that the radiation yield and power should both scale as I^2_{max}. We note that these ratios, listed in Table I, violate this scaling, possibly implying different convergences for each mass array.

The *plasma* convergence ratio (CR) in these experiments was estimated three independent ways, as illus-

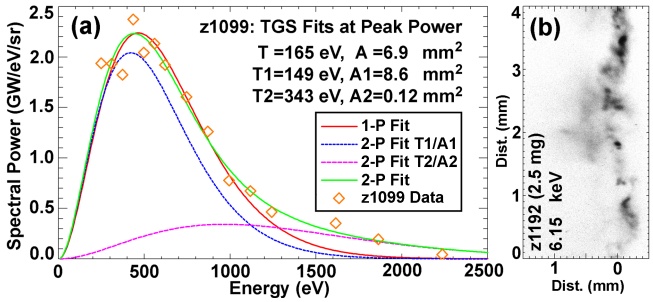

FIG. 5: (a) One- and two-Planckian fits to transmission grating spectrometer data from a 1.1-mg array. (b) Example time-integrated 6.15 keV emission image (∼20 μm resolution).

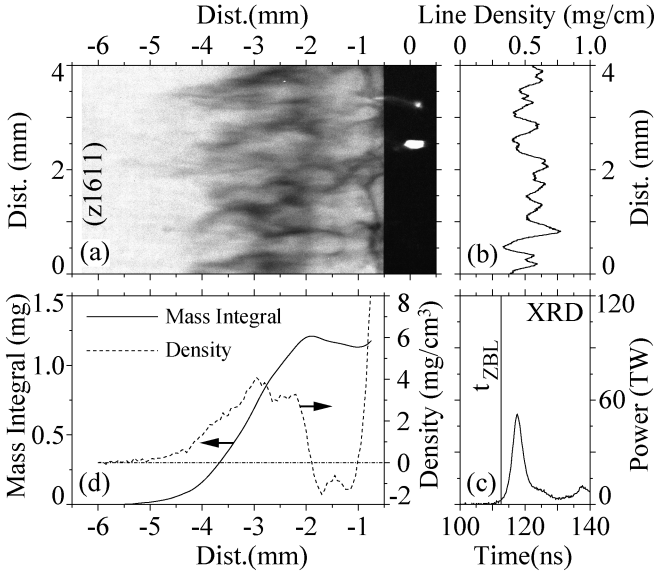

FIG. 6: Radiography data from the 1.1 mg array-on-rod test (z1611). (a) Image in transmission units (0-100%, black-to-white). (b) Inferred axial line density showing axial mass transport. (c) Timing of radiograph relative to x-ray power. (d) Density inferred from an Abel inversion of radiograph along with a running mass integral starting at r=6 mm. The negative density implies a violation of the cylindrical symmetry assumption, but the amount of mass involved is small.

trated by the example 1.1 mg array data in Fig. 4. Shot z1099 radiated 421 kJ in the main radiation pulse and 846 kJ total. For the measured peak current of 12.7 MA an average CR>30 (R_p <0.33 mm) is needed to get 421 kJ of kinetic energy (Fig. 3). At the time of peak power (frame 2 of Fig. 4a) 50% of the radiation is emitted within a 0.91-mm diameter region of the image, and 75% of the radiation is from a 1.8-mm region. Contours containing 50% and 75% of the total radiation are plotted for the grazing-incidence camera (GIK) data [15] in Fig. 4c, which is a continuous record of the axially-averaged, radially-resolved x-ray emission. These widths at peak power are 1.1 and 2.0 mm, respectively. Finally, the power plotted for the transmission grating spectrometer (TGS) [13] in Fig. 4d is inferred from a single-planckian fit to the data at each time. At peak power, a 165 eV plasma with an area of 6.9 mm^2 is inferred, corresponding to a diameter of 1.4 mm for the 5-mm tall aperture for that diagnostic. The plasma CRs inferred from these data are also plotted in Fig. 3.

The pinhole camera images consistently give the largest *plasma* CRs, yet for the 1.1 mg case it still falls short of the >30 *magnetic field* CR required to match the yield when compared with the most accurate estimates containing circuit models. The smaller GIK and TGS CRs are in closer agreement with one another. An example TGS spectrum from the 1.1 mg shot is shown in Fig. 5. From this we see that the GIK and TGS data are representative of the bulk of the soft x-ray emission with a peak near 450 eV, while the Be-filtered pinhole camera images (>1 keV bandpass) are representative of the high-energy tail of the spectrum (about 16% of the total energy radiated). This high-energy tail can be modelled using a two-planckian fit to the data in which a high-temperature, small-area blackbody radiates a comparable amount of energy to that emitted by the lower-temperature blackbody [13]. This high-energy tail and the axially peaked distribution of the self-emission might be consistent with the compression of some of the plasma by the magnetic field to small radii. Indeed, the *time-integrated* self-emission at 6.15 keV from these loads is generally confined to a sub-mm diameter column on axis and comes from numerous bright spots that are 50-300 μm in size. The example image shown in Fig. 5b is roughly consistent with a ∼340 eV, 0.12 mm^2 plasma (though it is from a different array mass). The maximum local diameter of the 6.15 keV emission at any given height of 0.4-0.5 mm, for a "CR">40-50!

In the tests with 1-mm rods, the rod limits both the plasma and magnetic field CRs to 20. The 1.1 mg shot (z1611) radiated 240 kJ during the main pulse and had a CR of 14 as inferred from the x-ray pinhole camera. Its energy vs. CR curves (not shown but similar to z1099) indicate about 310 kJ of magnetic work for a CR of 14, so the radiated energy on z1611 can be readily explained by the $\vec{j}\times\vec{B}$ energy and the difference could be energy lost in heating up the rod as noted later. The same conclusion holds for the other two array-on-rod tests, which had comparable CRs to z1611.

Considering only the main radiation pulse relevant to ICF, the emission data on bare-axis tests appears to show a discrepancy between the observed final plasma compression and that required for the $\vec{j}\times\vec{B}$ force to have done sufficient work to equal the radiated energy. After the main radiation pulse, when still more energy is radiated over a longer time scale, the plasma is also going unstable and the magnetic field can do more work as it drives two- and three-dimensional instabilities [16, 17]. Even during the main pulse when the plasma is relatively stable,

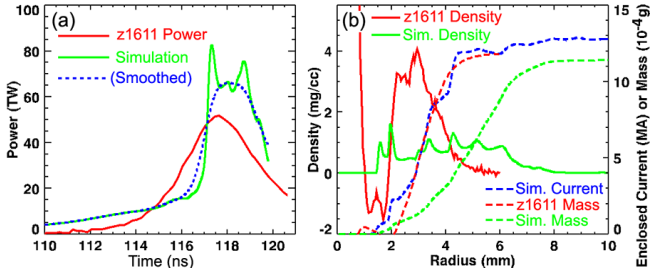

FIG. 7: (a) Comparison of simulated radiation power (including smoothing from instrument response) to the measured power on z1611. (b) Comparison of simulated and experimental density profiles and the enclosed mass/current inside each radius.

however, it is possible for the magnetic field to convect into the plasma and contribute additional energy to the plasma column [16]. Though our data is not conclusive as to the mechanism by which the full radiated energy during the main pulse is produced during bare-axis experiments, we note that the quantitative data presented here does bound potential mechanisms and simulations. We also note that the array-on-rod data represents the first clear case on the Z facility where the radiated energy could be explained by the observed $\vec{j} \times \vec{B}$ work done.

In addition to the amplitude, duration, spectrum, and size constraints to the radiation emission offered by the above data, in some cases further constraints from radiography are available. On the 1.1 mg array-on-rod test (z1611) we obtained a 6.151 keV radiograph [18] near stagnation, shown in Fig. 6, that had finite transmission everywhere in the image (the heavier arrays have opaque regions at this time). The on-axis rod also suppressed the time-integrated 6151±5 eV self-emission in most regions. This allowed us to Abel-invert an axially-averaged radial density profile from the radiograph for the first time.

The value of this systematic data set is illustrated by our attempts to simulate the 1.1 mg array-on-rod experiment (z1611). Two-dimensional (2D) r-z ALEGRA-HEDP magneto-hydrodynamic simulations were made using a mass-inflow boundary condition at the periphery which attempts to model the duration, amplitude, and axial variability of the mass ablation stage of wire-array implosions (a fully 3D effect otherwise). Such simulations produce qualitative features seen in these arrays experimentally such as plasma prefills inside the array [10] and trailing mass behind the main implosion front [18], as well as radiation powers and energies close to the experimental results (Fig. 7a). However, analysis of where the mass and current in the simulations are relative to the measured mass density (Fig. 7b) shows that the similarity in the duration of the radiation pulse may be largely because the width of the current sheath is approximately correct rather than the mass distribution.

Though the simulations produce a more distributed implosion front, they can assess the impact of the on-axis rod. About 0.24 mg/cm of Al plasma ablates from the rod before the main implosion front reaches the rod surface, but the plasma is tamped by the higher-velocity, ablated-prefill mass (about 40% of the total mass in these arrays, or 0.44 mg/cm here). The main impact of the ablated Al is that during the final 1 ns before the implosion reaches the rod the tungsten loses about 10% of its kinetic energy relative to a simulation without a rod. During the radiation pulse about 22% of the available energy goes into the internal energy of the rod. These numbers are consistent with the difference between the radiated energy and $\vec{j} \times \vec{B}$ work noted earlier for z1611.

Eventually we hope to use two-frame radiography to estimate not just the density profile but the velocity of the imploding mass, thereby estimating the peak kinetic energy just before stagnation, and thus by inference estimate the compressional work done on the plasma. We are also continuing to refine our computational models against the data set presented here and hope others will do likewise.

We thank C.A. Coverdale for reviewing the manuscript and D. Johnson, K. Keller, C.S. Speas, and I. Smith for diagnostic support on Z. Sandia is a multiprogram laboratory operated by Sandia Corporation, a Lockheed Martin Company, for the National Nuclear Security Administration under DE-AC04-94AL85000.

[1] P. J. Turchi and W. L. Baker, J. Appl. Phys. **44**, 4936 (1973).
[2] D. D. Ryutov, M. S. Derzon, and M. K. Matzen, Rev. Mod. Phys. **72**, 167 (2000).
[3] R. B. Spielman *et al.*, Phys. Plasmas **5**, 2105 (1998).
[4] M. E. Cuneo *et al.*, Phys. Plasmas **13**, 056318 (2006).
[5] T. W. L. Sanford *et al.*, Phys. Rev. Lett. **77**, 5063 (1996).
[6] C. Deeney, T. J. Nash, R. B. Spielman *et al.*, Phys. Rev. E **56**, 5945 (1997).
[7] M. K. Matzen *et al.*, Phys. Plasmas **12**, 055503 (2005).
[8] K. G. Whitney *et al.*, Phys. Plasmas **11**, 3700 (2004).
[9] D. L. Peterson *et al.*, Phys. Plasmas **5**, 3302 (1998).
[10] D. B. Sinars *et al.*, Phys. Plasmas **13**, 042704 (2006).
[11] W. A. Stygar *et al.*, Phys. Rev. E **69**, 046403 (2004).
[12] W. A. Stygar *et al.*, Phys. Rev. E **72**, 026404 (2005).
[13] M. E. Cuneo *et al.*, Phys. Rev. E **71**, 046406 (2005).
[14] S. V. Lebedev *et al.*, Phys. Plasmas **8**, 3734 (2001).
[15] D. F. Wenger *et al.*, Rev. Sci. Instrum. **75**, 3983 (2004).
[16] A. L. Velikovich *et al.*, Phys. Plasmas **7**, 3265 (2000).
[17] J. P. Chittenden *et al.*, Plasma Phys. Control. Fusion **46**, B457 (2004).
[18] D. B. Sinars *et al.*, Phys. Rev. Lett. **93**, 145002 (2004).